

Partially-Covered Fractal Induced Turbulence On Fins Thermal Dissipation

Soon Hong Chew

Monash University Malaysia

Su Min Hoi

Tunku Abdul Rahman University College

Manh-Vu Tran

Monash University Malaysia

Ji Jinn Foo (✉ Foo.Ji.Jinn@monash.edu)

Monash University Malaysia

Research Article

Keywords: Fractal geometry, Turbulence, Heat transfer, Plate-fin heat sink, Power spectra density, Vortex shedding

Posted Date: November 1st, 2021

DOI: <https://doi.org/10.21203/rs.3.rs-965861/v1>

License: © ⓘ This work is licensed under a Creative Commons Attribution 4.0 International License.

[Read Full License](#)

Partially-covered fractal induced turbulence on fins thermal dissipation

Soon Hong Chew^{1*}, Su Min Hoi², Manh-Vu Tran¹ and Ji Jinn Foo^{1*}

¹School of Engineering, Monash University Malaysia, 47500, Bandar Sunway, Malaysia

²Faculty of Engineering and Technology, Tunku Abdul Rahman University College, 53300

Kuala Lumpur, Wilayah Persekutuan Kuala Lumpur, Malaysia

*Corresponding author: soon.chew@monash.edu, Foo.Ji.Jinn@monash.edu

ABSTRACT

The impacts of partially-covered fractal grids induced turbulence on the forced convective heat transfer across plate-fin heat sink at Reynolds number $Re_{Dh}=22.0\times 10^3$ were numerically and experimentally investigated. Results showed that partially covered grids rendered a higher thermal dissipation performance, with partially covered square fractal grid (PCSFG) registering an outstanding increase of 43% in Nusselt number relative to the no grid configuration. The analyzation via an in-house developed single particle tracking velocimetry (SPTV) system displayed the findings of unique “Turbulence Annulus” formation, which provided a small degree of predictivity in the periodic annulus oscillations. Further assessments on PCSFG revealed the preferred inter-fin flow dynamics of (i) high flow velocity, (ii) strong turbulence intensity, (iii) vigorous flow fluctuations, (iv) small turbulence length scale, and (v) heightened decelerated flow events. Furthermore, power spectra density unveiled the powerful vortex shedding effect, with PCSFG achieving fluctuation frequency $f=18.5\text{Hz}$ close to an optimal magnitude. Such intricate flow structures pave the way for superior thermal transfer capabilities, benefiting the community in developing for higher efficiency heat transfer systems.

Keywords: *Fractal geometry; Turbulence; Heat transfer; Plate-fin heat sink; Power spectra density; Vortex shedding*

Introduction

Turbulences are described as flows that possess irregular, unpredictable and chaotic fluid motions. The formation of turbulence links closely to the behaviour of particles, whereby excessive kinetic energy in portions of fluid are able to overcome the viscosity effects that dampens flow fluctuations¹. It is encountered in everyday phenomenon and has great mixing capabilities due to intrinsic diffusive characteristics of increased rate of mass, momentum and energy transport. Such mixing properties heightened the flow-thermal boundary layers reconstruction and reshuffling probability, thus enhancing forced convection. To date,

33 multitudinous approaches had been conducted to unravel the heat transfer oriented flow
34 patterns. The usage of 2D planar space-filling fractal grids have seen an increase in reputation
35 for its effectiveness as a turbulator, owing to the feasibility of fine-tuning grid geometries in
36 expressing for a preferred thermo-fluid interplay.

37 The aforementioned planar fractal grids consist self-similar geometries of various
38 scales, with the pioneering study conducted by Hurst and Vassilicos². Recently, the turbulators
39 are seen in wide area of investigations, which includes but not limited to impinging jets³⁻⁵,
40 flame speed augmentation⁶, and energy harvesting^{7,8}. Square fractal grids (SFG) in particular
41 have been extensively researched due to the distinctive nature of turbulence production and
42 decay regions^{5,9}. It was reported that the turbulence generated from multilength-scale fractal
43 grids attained higher turbulence intensities and local flow Reynold number Re with reference
44 to a typical regular grid of similar or higher blockage ratio σ_r ^{10,11}. Wakes shed by the grid bars
45 of different length-scales meet at different downstream distances, and thus elongating the
46 turbulence production region. Such flow structures enable higher heat transfer capabilities.

47 However, the hindrance from multitudinous wake interactions could possibly retard the
48 airflow velocity. Hence, it raised the following questions: Is there any other fractal designs that
49 could better enhance heat dissipation performance? Will it be possible to maintain the
50 advantages of SFG induced turbulences, whilst improving heat sink thermal transfer, even at a
51 targeted localized region? What will be the corresponding fluid flow structures induced through
52 such newly designed grid? The outcome of these queries would propose a novel grid model
53 that would provide additional insights in the preferred flow dynamics for thermal dissipation.
54 For the current investigation, it was hypothesized that a vertical segmentation to SFG may
55 amass the production of highly positive thermal dissipation flow structures that is advantageous
56 for the forced convective heat transfer of a plate-fin heat sink, paving the way for the
57 development of high efficiency heat transfer systems.

58 **Methods**

59 Current investigation offers the means of acquiring an in-depth realization of positive
60 thermal dissipative flow characteristics. As such, numerical and experimental approaches will
61 be utilized to deduce and explain the grid-induced plate-fin heat transfer performances, as well
62 as the underlining inter-fin flow dynamics. Briefly, a transparent acrylic wind tunnel of
63 dimension $160 \times 160 \times 2560 \text{mm}^3$ was connected to a flow-straightened bell mouth inlet, with an
64 axial fan (Kruger, SG) paired along to ensure centreline inlet air velocity $U_0 = 2 \text{ms}^{-1}$,

65 corresponding to Reynold number of $Re_{Dh}=22.0 \times 10^3$. The current use of turbulator includes (a)
66 regular grid (RG), (b) square fractal grid (SFG), (c) partially-covered regular grid (PCRG) and
67 (d) partially-covered square fractal grid (PCSFG) as shown in Fig. 1(a-d), with no grid (NG)
68 configuration acting as the control. The grids enjoy similar blockage ratio $\sigma_r=0.49$ and details
69 of the grids' dimensions, i.e. thickness ratio t_r and fractal iterations N can be observed in Table
70 1. Each grid configuration together with a 1×4 rectangular plate-fin heat sink (aluminium 1100-
71 H14) of dimension $4 \times 20 \times 160 \text{mm}^3$ fabricated symmetrically to a comparable heated base plate
72 were positioned within the wind tunnel test section as shown in Fig. 1(e), with the inter-fin
73 spacing δ and grid-fin distance l deduced at 5mm and 10mm, respectively. A heater plate
74 (GUNT, DE) was utilized to provide constant base heat flux of $q''=6 \times 10^3 \text{Wm}^{-2}$. As such, the
75 instantaneous temperatures at locations illustrated in Fig. 1(f) were measured using seven T -
76 type thermocouples and recorded through a data logger (GL800,.US) for a span of five minutes
77 (steady-state). The average Nusselt number Nu of the plate-fin was then calculated with Eq. (3)
78 to empirically evaluate the performance of forced convection, as shown below:

$$D_h = \frac{4A_w}{P} \quad (1)$$

$$\Delta T = T_m - \frac{T_{in} + T_{out}}{2} \quad (2)$$

$$Nu = \frac{q'' D_h}{k_{air} \Delta T} \quad (3)$$

79 where D_h denotes the hydraulic diameter, A_w the wind tunnel cross-sectional area, P the cross-
80 sectional perimeter, T_m the mean temperature of plate-fin heat sink, T_{in} the inflow temperature,
81 T_{out} the outflow temperature, and k_{air} the air thermal conductivity.

82 **Table 1**

83 Parameters of the grids in Fig. 1(a-d).

Grid type	t_r	$N=1$		$N=2$		$N=3$	
		L_0 (mm)	t_0 (mm)	L_1 (mm)	t_1 (mm)	L_2 (mm)	t_2 (mm)
RG	1.00	160.00	5.76	-	-	-	-
PCRG	1.00	160.00	6.50	-	-	-	-
SFG	9.77	101.43	24.45	50.71	5.00	22.86	2.50
PCSFG	9.77	101.43	24.45	53.71	8.00	22.86	2.50

84 The setup was also modelled as a computational domain in numerical investigation
85 using the computational fluid dynamics (CFD) commercial software package ANSYS-Fluent
86 (ver..16.0, USA). Reynold Stress Model (RSM) was employed under the first order upwind
87 spatial discretization to offer the prediction of grid-induced turbulence. The convergence
88 criteria of residual 10^{-3} were prescribed for all the governing computational calculations, with
89 the exception of energy equation to be 10^{-6} . Details of the governing equations can be
90 referenced in Teh et al.¹². Besides, mesh independency test using finer tetrahedron elements
91 around the grid-fin conformation was also conducted, with maximum percentage difference of
92 0.48% recorded for Nu as the number of elements increased from 0.8×10^6 to 3.0×10^6 . In all
93 cases, reliable numerical outcomes were secured. Furthermore, two main parameters, namely
94 (δ , l), were explored for the design of experiment (DoE) to systematically observe the
95 individual influence and correlation with respect to grid-fin's $Nu(\delta, l)$. A total of 55 sampling
96 points were customary input to the design space, and Kriging regression was applied to predict
97 the response surface mapping with respect to CFD processed DoE data points.

98 Subsequently, a re-scaled transparent acrylic plate-fin setup (replacing aluminium heat
99 sink) was employed together with an in-house developed single particle tracking velocimetry
100 system (SPTV) to empirically capture grid-induced flow fluctuations. SPTV introduced the
101 means of investigating localized flow structures in a non-intrusive and inexpensive approach.
102 It captures the concatenating spatial position of a tracer particle that is lightly attached to a
103 polyester yarn fluctuating at an inter-fin 'local' region with a pair of synchronized high-speed
104 cameras [see Fig. 1(f)]. The particle was imaged by two coupled charged devices (CCD)
105 cameras (FLIR Integrated Imaging Solution Inc., CA) on top and side sections of wind tunnel
106 at 80fps, resulting in the compilation of 4.82×10^3 images per camera. Image processing and
107 correction methods were then performed using internally established MATLAB (R2016b, US)
108 algorithm to acquire highly contrast particle images that were exempted from cameras'
109 distortion, refractive and perspective misplays. Such features allowed for the accurate detection
110 of particle's centroid in consecutive images through built in computational algorithm. Through
111 comparison on the locality of tracer particle in successive images, the spatial position can be
112 reconstructed in a Cartesian coordinate system, where the particle's trajectory, velocity
113 fluctuations along with the underlining flow dynamics can be computed accurately. Details of
114 the calibration and correction processes are shown in the following sections.

116 Two synchronized high-speed cameras were calibrated to ensure the precise alignment
117 of optical axes at orthogonality with one another by incorporating a calibration platform
118 [see.Fig..2(a)]. The calibrator consisted of 77 white circles uniformly arranged at a 7×11 array
119 in both X - Y and X - Z planes, where frontal images of the circles were captured and analysed
120 using computational algorithm to attest for the maximum deviation of 0.10mm between optical
121 axis and platform centre, thus assuring parallelism of cameras' optical plane with the platform.
122 The intersection between the optical axes denotes the origin of the coordinate system, with
123 (x,y,z) representing the streamwise, spanwise and transverse directions, respectively.
124 Thereupon, the particle's fluctuating positions were captured. The individual time-series
125 images were further processed by an un-distortion algorithm in MATLAB single-camera
126 calibration toolbox to minimize distortion effects. Briefly, images of checkerboard with square
127 arrays of 5×8 were first recorded at 20 different orientations using the two cameras and
128 registered subsequently in the toolbox. Consequently, the calibration parameters, i.e. focal
129 length, optical centre and lens distortion coefficient were pinpointed, whereby a custom
130 algorithm was realized to undistort all images, securing the SPTV particle's spatial accuracy.

131 The aforementioned images were further processed to increase the contrast of the tracer
132 particle through background subtraction and bitonal conversion techniques. Individual pixels
133 of the images embodied a pixel value that varies between 0 (black) to 255 (white), with
134 numerals in between representing monochrome colour tones. Each pixelized value was
135 subtracted with the background (image with absence of tracer particle) to minimize background
136 noises. Subsequently, an intensity threshold was introduced to binarize the images, i.e. setting
137 pixel value above threshold to 1 (white) and vice versa, so that the contrast of tracer particle
138 was emphasized, thus attaining a high signal-to-noise image for particle identification. The
139 centroid of the particle was then determined by employing circular Hough transform, which is
140 accessible through the MATLAB built-in function.

141 The centroid of tracer particle determined at current stage is subjected to refractive and
142 projection errors. As the correction processes for both cameras are similar, only the side camera
143 will be referred in the discussions hereafter. Note that coordinate notations (x, z) are utilized
144 for side camera and (x, y) for top camera. Concisely, refractive errors occur due to the bending
145 of light as it passes between mediums of different optical densities. The detected particle
146 positions will be observed to offset from the actual position, as illustrated in Fig. 2(b). As such,

147 a corrective module that utilizes Snell's law had been incorporated into the MATLAB
 148 algorithm to tackle the inaccuracies. The equations utilized in the module are observed as below:

$$\bar{R} = \sqrt{(x_d - x_c)^2 + (z_d - z_c)^2} \quad (4)$$

$$\theta_1 = \tan^{-1} \left(\frac{\bar{R}}{y_D + y_w + y_l} \right) \quad (5)$$

$$\theta_2 = \sin^{-1} \left(\frac{n_1 \sin \theta_1}{n_2} \right) \quad (6)$$

$$R = y_D \tan \theta_1 + y_w \tan \theta_2 + y_l \tan \theta_1 \quad (7)$$

149 where (x_c, z_c) represents the coordinates of optical centre, (x_d, z_d) the camera detected particle
 150 centroid, \bar{R} the observed displacement from optical centre, y_D the detected horizontal particle-
 151 to-wall distance, y_w the acrylic wall thickness, y_l the horizontal lens-to-wall distance, (θ_1, θ_2)
 152 the Snell's law angles, (n_1, n_2) the refractive indices of (air, acrylic), and R the corrected
 153 displacement from optical centre. Briefly, the (x_d, z_d) were coded as the input to initiate a series
 154 of computational equations that allowed for the R to be acquired. Intrinsically, coordinates
 155 corrected for refractive error (x_r, z_r) can be determined through rationalizing for similar
 156 triangles, and are computed as follow:

$$x_r = x_c + (x_d - x_c) \cdot \frac{R}{\bar{R}} \quad (8)$$

$$z_r = z_c + (z_d - z_c) \cdot \frac{R}{\bar{R}} \quad (9)$$

157 On the other hand, the perspective distortion caused different magnification of particle
 158 image in relative to the distance from lens [see Fig. 2(c)]. Notably, the pixel-to-distance ratio
 159 varied at different planar locations, where particle situated closer to the lens would appear to
 160 be enlarged, and a small shift in particle coordinate would emerge as a large motion as detected
 161 by camera. Such repercussions were minimized by uncovering the perspective projection
 162 equations. Generally, all the time-series images of tracer particle were perceived to be projected
 163 onto a focusing frame coincident with the calibration platform. Since the dimensions of the
 164 calibration platform were discerned, the metric distance of the particle from optical centre can
 165 be calculated through pixel-to-length conversion. By locating the depth of particle in relative
 166 to the camera lens, the correct metric scale can be determined, hence an accurate spatial
 167 coordinate reconstruction can be computed as below:

$$x_a = \frac{y_D + y_w + y_l}{y_f + y_w + y_l} (x_r - x_c) + x_c \quad (10)$$

$$z_a = \frac{y_D + y_w + y_l}{y_f + y_w + y_l} (z_r - z_c) + x_c \quad (11)$$

168 where y_f represents the frame-to-wall distance, and (x_a, z_a) the calculated coordinate of the
169 tracer particle.

170 For the algorithm to be fully functional, the information for y_D is imperative. However,
171 said variable obtained directly from the top camera would still be subjected to perspective
172 errors. Therefore, geometrical formula is used to pinpoint the y -coordinate (y_a) of the particle
173 such that the inaccuracy of y_D can be minimized. By observing on Fig. 2(d, e), the (y_a, z_a)
174 coordinates can be related by similar triangle equations:

$$y_{a+1} = \frac{y_r - y_c}{z_l + z_w + z_f} (z_l + z_w + 0.5z_f - z_a) + y_c \quad (12)$$

$$z_{a+1} = \frac{z_r - z_c}{y_l + y_w + y_f} (y_l + y_w + 0.5y_f - y_a) + z_c \quad (13)$$

175 An iterative method had been utilized until both coordinates converge with a criteria of
176 $\varepsilon=1.0 \times 10^{-2}$ mm. Combining information from both cameras, an accurate particle coordinate
177 (x_a, y_a, z_a) can finally be realized. As such, the instantaneous velocity fluctuation in the three
178 different directional components can be computed. It was calculated by the change of
179 displacement over a small time interval between frames, through the equations listed below:

$$u' = \lim_{t_2 \rightarrow t_1} \frac{x_2 - x_1}{t_2 - t_1} \quad v' = \lim_{t_2 \rightarrow t_1} \frac{y_2 - y_1}{t_2 - t_1} \quad w' = \lim_{t_2 \rightarrow t_1} \frac{z_2 - z_1}{t_2 - t_1} \quad (14)$$

180 where u' , v' and w' denote the velocity fluctuations in the (x, y, z) directions, t the image
181 timestamp and subscript (1, 2) the parameters on the current and subsequent frame, respectively.
182 The employment of SPTV allows for the detection of turbulence characteristics, and are further
183 extracted for analysis purposes.

184 **Results and Discussions**

185 *RSM and SPTV validation processes*

186 In order to confirm the numerical accuracy of current RSM in revealing the
187 fundamentals of insert-induced turbulence upon fins forced convection, careful validation
188 using Hoi et al.'s^{13,14} experimentally recorded measurements are conveyed. Fig. 3(a)
189 demonstrates the comparison between the experimental study of NG and SFG induced Nu with
190 present numerical simulation. Evidently, small percentage differences of 0.34% and 0.19% are
191 recorded for NG and SFG, respectively. Likewise, fractal grid generated flow dynamic, namely,
192 the centreline streamwise flow velocity U_c is as well validated and compared with experimental
193 data. It is seen in Fig. 3(b) that the normalized flow velocity at the lee of grid decreases $\times 0.28$
194 nonlinearly, i.e., from about $U_c/U_0=1.9$ to 1.4, with a maximum discrepancy of 6.15% recorded
195 between the numerical and experimental results. Such subtle documented differences in
196 Fig. 3(a, b) indicate that the RSM simulated forced convection and fluid flow fits practically
197 well with the experimental study. Hence, it is justified that the current use of numerical scheme
198 is capable of predicting grid-induced flow dynamic in aiding the thermal dissipation of plate-
199 fin heat sink with reasonable accuracy.

200 Similarly, validation on the accuracy of the current SPTV coordinate detection and
201 reconstruction system is also conducted. The SPTV tracer particle had been manually
202 complemented into the wind tunnel test section at known spatial positions. Fig. 3(c)
203 demonstrates the careful arrangement of tracer particle along the (x, y, z) axes, with each
204 placement bearing a step size of 1cm, expanse from the origin. Subsequently, particle images
205 are recorded at each coordinate and analysed using MATLAB algorithm, whereby the error
206 margins can be computed [see Fig. 3(d)]. Clearly, the maximum percentage errors attained for
207 each directional component are discerned to be 1.49%, 1.69%, and 1.62%, respectively, which
208 corresponds to the highest recorded inaccuracy of 5.0×10^{-2} cm. Such minute misplays imply a
209 high accuracy and reliability in spatial reconstruction, thus validating the accuracy of current
210 SPTV in coordinate detection.

211 *Effects of δ and l on fins forced convection*

212 From the numerical study, the correlations between δ and l upon plate-fin heat sink
213 forced convection at $Re_{Dh}=22.0 \times 10^3$ are acquired. As seen in Fig. 4(a), the RG induced Nu
214 expresses its unique forced convection as a function of $Nu(\delta, l)$ with a wider high Nu coverage
215 amongst all grid configurations that spans between $4.0\text{mm} \leq \delta \leq 35.5\text{mm}$ and $10\text{mm} \leq l \leq 75.5\text{mm}$.

216 RG achieved a rather consistent Nu distribution, owing to the uniform t_0 assignment that
217 generates wakes of highly homogenous and isotropic turbulence accompanied with lower flow
218 dynamic disturbance. Such weaker wake interplays lessen the disruption to flow boundary layer
219 along each fin, hence justifying the all-around lower capability in promoting thermal
220 dissipation. On another note, SFG is observed to attain an extensive high Nu coverage in
221 comparison with RG, but smaller in the expanse of partially-covered grids [see Fig. 4(b)]. Such
222 enhancement in Nu contrasting to RG is likely to be contributed via the multi-length scale
223 interactions of wakes that originated from SFG's variety fractal bar thicknesses. Clearly,
224 increasing the parameters (δ, l) is observed to have deteriorating effects in Nu, indicating that
225 the thermal dissipation performance is highly sensitive to the tuning of δ and l . Moreover, a
226 weak Nu regime is determined at the span of $15\text{mm} \leq \delta \leq 25\text{mm}$ and $10\text{mm} \leq l \leq 14\text{mm}$. The
227 phenomenon manifests similar observation in preceding findings¹⁵, where the deterioration is
228 instituted from weak turbulence intensity and low flow velocity between fins.

229 Interestingly, PCRG and PCSFG are able to realize an effective domain of high thermal
230 dissipation, with higher $Nu(\delta, l)$ discerned around $4\text{mm} \leq \delta \leq 10\text{mm}$ for the former and
231 $4\text{mm} \leq \delta \leq 12\text{mm}$ the latter [see Fig. 4(c, d)]. The integration of larger t_0 -induced wakes
232 (see Table 1) accompanied with fluid flow acceleration through the vertically aligned
233 separation generates beneficial hydrodynamic interactions which gives rise to intense forced
234 convection. Notably, the Nu is less sensitive towards l . The partially-covered grids induced
235 flow perturbation brings about the highest local acceleration immediately leeward from grid.
236 The lengthening of l increases the jet mixing in terms of spanwise and streamwise flow
237 dynamic dissipation and diffusion which eventually retard slightly the fins' thermal transfer.
238 Yet, Nu decreases with increasing δ . The penetration of flow fluctuations into fins' flow
239 boundary layer may have been gradually weakened at larger δ , which supports unwanted fluid
240 bypass. Surprisingly, PCSFG is able to mitigate the shortcoming of SFG, where the lowest Nu
241 generated is observed at a region of much larger δ and l (blue). The high flow velocity
242 penetrated through the perforations and central void reinforces the favourable multitudinous
243 wake interactions initiated from fractal bars of different length scale, effectively empowering
244 thermal dissipation performance. In general, the 2D Nu contours suggest that the
245 implementation of partially-covered grids are capable of providing higher thermal dissipation
246 even at a wider δ . Hence, the optimum $\delta=5\text{mm}$ and $l=10\text{mm}$ is empirically evaluated in the
247 next section for a deeper insight on the various grid-induced flow dynamics.

249 Undoubtedly, the experimentally proven highest $Nu=4341.7$ is achieved using PCSFG
250 as shown in Fig. 4(e), with a remarkable percentage enhancement of 42.9%, as compared with
251 the control NG. The augmentation in Nu is followed by PCRG, SFG, and RG ranked in
252 descending order, with the percentage increase recorded as 29.2%, 21.0% and 12.8%,
253 respectively. The attainment of Nu induced from different turbulators are comparable to the
254 numerical results performed through RSM, thus uncovering the value of simulated studies in
255 predicting for the trend of forced convective heat transfer on plate-fin heat sink through various
256 2D planar grids. Clearly, the current uses of partially-covered grids are superior to their classic
257 grid counterparts in terms of heat transfer, suggesting the implementation of a vertical mid-
258 plane separation incites favourable flow dynamics that support forced convection.

259 On another note, the localized Nusselt number Nu_L at locations mentioned in Fig. 1(f)
260 are illustrated in Fig. 4(f, g) to identify the locations with the utmost heat transfer. Interestingly,
261 the Nu_L displayed at the base of plate-fin for all grid configurations showed symmetry,
262 whereby the Nu_L surges at the base of mid fin (position 2). The highest achieved $Nu_L(2)$ is
263 recorded for SFG owing to the presence of thick t_0 assignment, which generates wakes of
264 sizeable length-scale near the base region for vigorous thermo-fluid interplay. Yet, the effects
265 slowly diminished as we shift the position to centreline, whereby PCSFG is now observed in
266 Fig. 4(g) to dominate the forced convection through realization of potent Nu_L at inter-fin
267 regions (positions 4, 5 and 6). In spite of the high attainment of Nu_L , a steep decline is observed
268 near the outer-fin surface (position 7) for SFG, PCRG and PCSFG. Current phenomenon might
269 indicate the diverging of airflow afar from fins' exterior, owing to the growth of flow boundary
270 layer at leading edge of outer-fins. However, a dissimilar phenomenon is observed for RG,
271 where $Nu_L(7)$ is noticed to be comparable with $Nu_L(5)$ but demonstrate a deterioration in $Nu_L(6)$.
272 The evenly separated RG perforations with uniform t_0 generated an alternating region of high
273 and low airflow velocity U lee of grid, producing an imprint of t_0 in dissociating for retardation
274 of flow. Such imprint is projected streamwise towards the fin, with position 6 likely to be
275 coincident with it. The low flow kinetic energy reduces the likelihood of flow reshuffling, thus
276 sabotaging the plate-fin local thermal dissipation. On another note, positions (5, 7) are
277 integrated at the immediate region behind grid perforations, which surges the Nu_L due to the
278 heightened flow acceleration. Nevertheless, the forced convection is noticeably greater at the
279 mid of fins, i.e. positions (2, 5) for all grid conformations. Therefore, the SPTV tracer particle

280 is implemented at centreline $x/D_h=0.125$ to investigate the flow dynamics that dominates
281 thermal transfer processes.

282 *Empirical flow dynamics at localized inter-fin region*

283 Fig. 5(a) illustrates the U normalized with U_0 , i.e. U/U_0 induced through the different
284 2D planar grids. The U is gauged by means of a hotwired anemometer (Testo 405i, DE) at
285 centreline $x/D_h=0.125$ in the absence of plate-fin array. Notably, the U/U_0 generated through
286 various grids exhibit similar trend as the Nu , with $U(\text{PCSFG}) > U(\text{PCRG})$, and $U(\text{SFG}) > U(\text{RG})$.
287 It is renowned that the implementation of turbulator allows the acceleration of air flow due to
288 the sudden contraction of flow passage. The introduction of a vertically aligned separation in
289 the partially-covered grids promotes mid-plane jet formations, owing to the principle of mass
290 conservation. Such separation effectively reduces the undesirable fluid bypass around the plate-
291 fins, and forcefully regulates the working fluid to penetrate inter-fin regions. In addition, the
292 accelerated airflow in between the fin array enforces greater wall shear stress along fin surfaces,
293 which limits the growth of viscous sub-layer, thus effectively enhancing forced convection.

294 Even though the mid-plane separation is employed on both PCRG and PCSFG, a
295 greater heat dissipation is still documented for the latter. The enhancement in Nu for PCSFG
296 contrasting with PCRG may be due to the multi-length scale wake interactions via the
297 multiplicity of fractal bar thickness. As reported earlier^{9,16}, the interplay between accelerated
298 airflow and wake structures through the variety of fractal bar thickness promotes generation of
299 multi-length scale turbulent eddies. Small-scale eddies induced through thinner fractal bars are
300 described to effectively facilitate plate-fin heat dissipation through flow dynamic energy
301 cascading. The formation of anisotropic and inhomogeneous eddy structures encompassing a
302 collection of sizes and frequencies increase the likelihood to the disruption of flow boundary
303 layers along the fin. On the contrary, PCRG engenders weaker flow agitation capabilities due
304 to the isotropic and homogenous turbulence formation by uniform t_0 assignment. With the
305 current employment of PCSFG, effects of conventional fractal grids with the added benefit of
306 pronounced airflow acceleration at a localized region are amalgamated. The critical fragments
307 of turbulent eddies may be filtered along the inter-fin regions, coupling with the high U/U_0
308 triggers the active reshuffling of flow boundary layers, thus expounding the event where
309 $Nu(\text{PCSFG}) > Nu(\text{PCRG})$.

310 Besides, 2D-planar turbulators generate wakes with intensified shear layers that lead to
311 the formation of turbulence eddies. In order to quantify the regional turbulence intensity I , the
312 root mean square of velocity fluctuations detected from SPTV is rationalized with U_0 :

$$I = \frac{\sqrt{\frac{1}{3}(\langle u'^2 \rangle + \langle v'^2 \rangle + \langle w'^2 \rangle)}}{U_0} \quad (15)$$

313 where $\langle u'^2 \rangle$, $\langle v'^2 \rangle$ and $\langle w'^2 \rangle$ represent the ensemble average of squared velocity fluctuations
314 in (x, y, z) directions, respectively. As illustrated in Fig. 5(b), the paradigm demonstrated by I
315 for the various grids followed closely to that of Nu , implying a positive correlation in between
316 the two, i.e. higher I give rise to greater Nu . Evidently, the I induced from partially-covered
317 grids are comparably more intense than that of the fully-covered grids, thereafter the control
318 NG. The raised level of I documented for PCSFG and PCRG may be due to the restructuring
319 of wake dimensions through implementation of a vertically-aligned separation, providing the
320 energy necessary for vigorous turbulent eddies to infiltrate inter-fin regions.

321 In order to conceptualize the effects of I induced from various grids, the trajectories of
322 the tracer particles are demonstrated in Fig. 6(a, b), with the former representing the Y - Z plane
323 (cross-sectional view) and latter representing the X - Z plane (side view). Clearly, smaller
324 fluctuations are observed for NG and RG configurations, whereby the frontal coverage areas A
325 with respect to Y - Z plane are recorded at a minimum of 1.2mm^2 and 1.4mm^2 , respectively.
326 Through the amalgamation of fractal bars, SFG is observed to attain a greater $A=2.9\text{mm}^2$ that
327 fairly resembles the shape of a crescent. Interestingly, both partially-covered grids develops an
328 elliptical structure from the particle's trajectory, which would be fitting to address it as a
329 'Turbulent Annulus'. The formation of the annulus may signify the generation of new and
330 unique flow structures, as it displays small degree of predictability in the particle's periodic
331 annulus oscillations, despite the chaotic nature of turbulence. Nevertheless, higher fluctuation
332 amplitude is observed from PCRG and PCSFG generated particle trajectory, especially in the
333 y - and z - directions, which are vital in disturbing the flow and thermal boundary layers.
334 Remarkably, the A of PCRG is greater than PCSFG despite the lower I attainment. Distinct
335 flow dynamics induced from PCSFG consolidated the particle's trajectory to a rather dense and
336 intense flow fluctuation around the sizable annulus. Unlike for PCRG, which has a smaller
337 dimension along with diffusive characteristic at the annulus interior. Such diffusive effect
338 disperses flow energy to undesirable areas, thus retarding heat transfer processes.

339 To further describe for the fluctuation intensities, cumulative probability (CP)
340 distribution on the v'^2 and w'^2 for the variety of turbulators are depicted in Fig..5(d, e). As
341 shown in Fig. 5(d), NG and RG have a small range of spanwise fluctuations, whereby 95% of
342 v'^2 less than $3.8\text{m}^2\text{s}^{-2}$ and $10.7\text{m}^2\text{s}^{-2}$ are recorded, respectively. It showed a vast difference with
343 SFG as 95% of v'^2 is below $233.8\text{m}^2\text{s}^{-2}$, implying a great elevation in fluctuation amplitude.
344 However, the strength is still inferior to the partially-covered grids, with PCSFG recorded with
345 a higher probability of stronger fluctuations approximately between $80.0\text{m}^2\text{s}^{-2} < v'^2 < 440.0\text{m}^2\text{s}^{-2}$
346 as compared to PCRG. Likewise in Fig..5(e), the overall w'^2 trend depicted minor differences
347 with v'^2 , where a clear distinction of wider w'^2 variations are still observed for PCSFG, along
348 with PCRG, SFG, RG and NG ranked in descending order. The event is apparent at the top five
349 percentile, as PCSFG realized the highest variation of $w'^2 > 381.1\text{m}^2\text{s}^{-2}$. The pronounced v' and
350 w' give rise to greater development of A , suggesting a larger area of flow boundary is being
351 agitated at the localized inter-fin region, thus poses a unique advantage in supporting potent
352 thermal dissipation.

353 In the case of turbulent airflow, the effects of turbulence length scale L on the forced
354 convective heat transfer should be considered as well, as it unveils critical thermo-fluid
355 interplay upon heat exchanger thermal transfer^{9,16}. L provides a representation of spatial
356 dimension for turbulent vortices. Such L are computed by integrating the normalized
357 autocorrelation function of velocity fluctuation with respect to the time-lapse, using Eq. (17):

$$R_{f'}(t) = \frac{\langle f'(t)f'(t + \tau) \rangle}{\langle f'(t)^2 \rangle} \quad (16)$$

$$L = U_0 \int_0^T R_{f'}(t) d\tau \quad (17)$$

358 where $R_{f'}$ represents the normalized autocorrelation function of velocity fluctuation, f' the
359 directional components of velocity fluctuations (u' , v' , w'), τ the time-lapse, T the first zero-
360 crossing of $R_{f'}$, and $\langle . \rangle$ the ensemble average. The L generated from the different 2D-planar
361 grids are rationalized with δ , i.e. L/δ and is shown in Fig. 5(c).

362 Unsurprisingly, the NG induced L/δ in (x, y, z) directions are realized to be the highest.
363 The straightened airflow is only subjected to wall shear stresses from wind tunnel surfaces,
364 which lacks flow obstructions prior to plate-fin filtration, hence higher L/δ . Conversely, the L/δ
365 is substantially reduced with the use of space-filling grids: a direct consequence of grid bars in
366 filling the planar spaces. Interestingly, RG and SFG developed a comparable $L(z)/\delta$, but are

367 contrasting in reference to streamwise and spanwise L . The event suggests that a sizeable $L(y)/\delta$
368 by SFG is preferred for forced convection since $Nu(SFG) > Nu(RG)$, and could be enforced
369 through the realization of smaller $L(x)/\delta$. By considering vortices rotating in the X - Z plane, the
370 dwindling $L(x)/\delta$ may increase the vortices' angular velocity around y -direction ω_y , but in turns
371 extending the vortex line laterally due to the conservation of angular momentum, i.e. vortex
372 stretching. The elongation of vortex structures thus effectively interacts and disrupts the fins'
373 boundary layer. The aforesaid implication concurred closely with RG, yet poses an opposite
374 effect of streamwise elongation, which lessened boundary layers' agitation probabilities.

375 Nevertheless, an overall small L/δ is still favourable for forced convective heat transfer,
376 since partially-covered grids are noticed to induce a relatively small and uniform L/δ . The
377 findings are supported with reference to previous literatures^{15,17-19}, whereby higher heat transfer
378 is usually achieved at lower L . The contraction of flow due to the two partially-covered grid
379 segments positioned along each side of wind tunnel could have developed a profound amount
380 of similar yet counter-rotating pair of vortices. The vortex pair that oppose in motion maximize
381 the straining of airflow, which induces highly intense eddies with smaller diameters. Such
382 development of eddies could possibly be sorted along the fin surfaces, and promotes heat
383 transfer through flow dynamic energy cascading.

384 In general, the coupling effect of $(U_{high}, I_{high}, L_{low})$ as demonstrated from PCSFG
385 induces flow structures that are favourable in enhancing heat transfer. The results expressed in
386 the current section showed that SPTV is viable to provide informative data to describe for the
387 preferred thermal dissipation flow dynamics. However, one might wonder if the investigation
388 on a targeted localized region using SPTV particle at centreline of inter-fin is sufficient to
389 conclude for the whole plate-fin array. Hence, numerical predictions are utilized in the
390 following to describe for the overall flow dynamics at inter-fin in terms of isosurfaces and 2D
391 contours to append for the limitations of current experimental findings.

392 *Simulated flow properties at inter-fin region*

393 The isosurfaces of (i) $U/U_0=2.38$, (ii) $I=0.33$ and (iii) 2D contour of L at $x/D_h=0.125$
394 are demonstrated in Fig. 7 to predict the underlying flow dynamics at a more pronounced inter-
395 fin region. By focusing on RG in Fig. 7(a), it is noticed that the high U/U_0 is unlikely to
396 penetrate through the plate-fin array. The evenly distributed perforations of RG generated low
397 flow acceleration that is rapidly dissipated and dispersed with the surrounding tardy fluid
398 momentum leeward of grid, disabling high U/U_0 to be regulated into the inter-fin separations.

399 Besides, the isosurface distribution of strong I in Fig. 7(b) is perceived to be partitioned into
400 segments, with bigger voids arising between the second and third fins, owing to the t_0 imprints
401 from windward grid geometry.

402 Moving on to SFG, it is noticed that the 3D isosurface of U/U_0 in Fig. 7(d) is able to
403 penetrate well through the inter-fin separations. The incorporation of airflow that forced
404 through SFG of thicker t_0 in conjunction with the unevenly distributed fractal dimension
405 significantly stimulates the jet flows, producing working fluid of high flow velocity to
406 predominantly infiltrate through the fin-array. Such flow structure increases the likelihood of
407 flow perturbations, which contributed to the isosurface distribution of strong I as shown in
408 Fig. 7(e). Interestingly, the isosurface distributions for both U/U_0 and I are perceived to inhibit
409 high isosurface porosity, with voids scattered towards the upper and bottom portions of each
410 inter-fin. The flow recirculated in the lee from fractal bars incurs considerable flow retardation,
411 yielding an imprint of t_0 dissociated isosurface. The amalgamation of such transition between
412 the potent and frail interfaces may lessen the possible reshuffling of flow and thermal boundary
413 layers along fins, which sabotage the local thermal dissipation.

414 Conversely, highly uniform U/U_0 isosurface scattering for the PCRG and PCSFG can
415 be distinctly seen in Fig. 7(g, j), respectively. Apprehensively, jets are not only created and
416 accelerated through the insert perforations via the sudden introduction of an incompressible
417 grid, most importantly, the flow dynamics are as well simultaneously amassed around the mid-
418 plane segmentation, which allows the air to speed up and penetrate deeper and more uniformly,
419 hence increasing the scalar and flow momentum transportations. Moreover, denser isosurface
420 distribution density can be clearly perceived with PCSFG as to PCRG. Notably, minor
421 discontinuities are recorded for the former in comparison SFG, suggesting the effect of
422 multitudinous wake interactions in lowering down the flow velocity has been significantly
423 mitigated. The strong I distributions of PCRG and PCSFG are of greater extent with seemingly
424 the least variation in terms of respective uniformity [see Fig. 7(h, k)]. Through effective
425 coupling between the grid-induced turbulence and downstream plate-fin array, it initiates the
426 second stage of flow eddies filtration, which leads to a predominant, unique fluid flow
427 fluctuation along with potent flow dynamics to penetrate into fin-array. As a result, PCRG and
428 PCSFG empower vigorous fin-wake interplay which effectively heighten forced convection.

429 Furthermore, the numerically calculated 2D L contours generated by the various grid
430 conformations are investigated as well. Such numerically computed L is defined as²⁰:

$$L = \frac{C_\mu^{3/4} \kappa^{3/2}}{\varepsilon} \quad (18)$$

431 where κ denotes the turbulence kinetic energy, ε the turbulence eddy dissipation rate, and C_μ a
432 model constant of $C_\mu=0.09$. From Fig. 7(c, f), RG configuration is clearly seen to incite the
433 largest inter-fin L , whereas domain of non-uniformity can be observed with SFG. Admittedly,
434 the region of high L of both grids are associated with the corresponding t_0 of the windward grid
435 geometry. The sizable span of t_0 gives rise to wakes of greater length scale, which generates
436 substantial shear levels and subsequently bigger eddies via wake-flow hydrodynamic interplays.
437 Conversely, SFG's smaller scale fractal bars promote the production of smaller eddies, that
438 may be potentially filtered and disseminated to the t_0 imprint complement regions. Interestingly,
439 the small-scale eddies are determined in Fig. 7(i, l) to propagate and uniformly distributed for
440 PCRG and PCSFG, similar to preceding findings in Fig. 5(c). The absence of first iterative
441 fractal bar in the mid-plane segmentation eradicates the accumulation of high length scale
442 wakes, thus preventing the formation of large turbulent eddies directly windward of fins. Most
443 importantly, miniscule yet vital fragments of turbulent eddies are found to approach and
444 attached actively along fin surfaces, which may effectively facilitate plate-fin heat transfer
445 through flow energy cascading, hence enhancing the forced convection process. In general, the
446 amalgamations of $(U_{\text{high}}, I_{\text{high}}, L_{\text{low}})$ are determined to be the favourable characteristics for
447 potent thermal transfer processes. Such numerical findings coincide closely with empirically
448 detected flow dynamics at centreline $x/D_h=0.125$, justifying the current use of SPTV in
449 describing for the positive thermal dissipation flow properties. Hence, statistical analysis is
450 conducted subsequently for a rigorous analyzation on grid induced flow characteristics.

451 *Statistical analysis of turbulent flow*

452 With the empirical computation of tracer particle's velocity fluctuations, it is possible
453 to calculate the acceleration of particle for each directional component with the formula below:

$$a_x = \lim_{t_2 \rightarrow t_1} \frac{u'_2 - u'_1}{t_2 - t_1} \quad a_y = \lim_{t_2 \rightarrow t_1} \frac{v'_2 - v'_1}{t_2 - t_1} \quad a_z = \lim_{t_2 \rightarrow t_1} \frac{w'_2 - w'_1}{t_2 - t_1} \quad (19)$$

454 where, a_x , a_y , and a_z represent the particle accelerations in the (x, y, z) directions, respectively.
455 Skewness S and kurtosis K , which represent the symmetricity and the extremities of data
456 distribution, are utilized to statically analyse the acceleration components induced from the
457 planar grids [see Fig. 8(a, b)]. It is computed in accordance with the equations:

$$S = \frac{\langle a_i^3 \rangle}{\langle a_i^2 \rangle^{\frac{3}{2}}} \quad (20)$$

$$K = \frac{\langle a_i^4 \rangle}{\langle a_i^2 \rangle^2} \quad (21)$$

458 where, i denotes the (x, y, z) directional components.

459 Undeniably, $S=0$ and $K=3$ represent the Gaussian distribution of data. It is noticed in
 460 Fig. 8(a, b) that the acceleration distributions are rather normally distributed for NG and RG,
 461 but with a slight positive skew, where $S(\text{NG}) < S(\text{RG})$ in all acceleration components. Such
 462 results signify an increase in accelerated flow for RG as compared to NG, especially in the
 463 streamwise direction. Clearly, a non-Gaussian behaviour is realized for SFG, PCRG and
 464 PCSFG, whereby $(|S| > 0, K > 3)$ are recorded for the former, and $(|S| > 0, K < 3)$ for the latter duo.
 465 The $\pm S$ achieved by SFG implies extreme decelerated turbulent events documented in the $(x,$
 466 $y)$ directions, along with turbulent accelerations in z -direction. These accelerations are
 467 considered to be rare and intensive, as indicated with the high positive $K > 3$. Interestingly,
 468 similar S developments are recorded for the partially-covered grids, but vastly disparate in K
 469 as evident from Fig. 8(b). The realization of $K \approx 2$ for PCRG and PCSFG depicts an increase in
 470 likelihood for the extreme decelerated (a_x, a_y) turbulent events, which could very well imply
 471 the high occurrences of alternating flow directions that escalates to the formation of copious
 472 vortices.

473 Undoubtedly, PCSFG is seen to manifest the highest negative skewness of $S = -0.12$ for
 474 a_y , which may suggest the preference for exhibiting extreme decelerated flow structures in the
 475 lateral direction for a strong thermo-fluid interplay between highly potent and numerous
 476 collaborative vortices. The comparable negative $S(a_x, a_y)$ indicated the small L eddies are
 477 compacted with intense X - Y plane flow circulations. Such high occurrences of dense and
 478 powerful eddies accompanied with minor vertical accelerations enable an extended exposure
 479 to the reshuffling of fins' boundary layer, thus generating highly positive thermal dissipation
 480 flow structures. Even though PCRG exhibits greater negative $S(a_x)$, it is deprived in the vital
 481 negative $S(a_y)$, consequently dampens the strength of flow circulation and forced convection
 482 capabilities. Nevertheless, the greater displays of such events as compared with SFG allow for
 483 $\text{Nu}(\text{PCRG}) > \text{Nu}(\text{SFG})$, even though the numeral polarity of S registered similarity. Conversely,
 484 NG and RG demonstrated moderate flow circulations, hence the low Nu. In general, the
 485 extreme decelerated flow events are capable of forming intense flow vortices, which is

486 beneficial in disruption of fins' boundary layer. Further research is still required to uncover the
487 S and K profiles at different inter-fin locality, in order to uncover the overall flow structures
488 that are preferable for maximising forced convection of plate-fin heat sink.

489 *Power spectra density (PSD)*

490 When comparing the effects of various grids in their heat transfer performance, it is
491 relevant to consider the PSD of flow, which deciphers the strength of velocity fluctuations in
492 accordance with the frequency domain. Such feat is achieved by utilizing Fourier transform on
493 the non-normalized autocovariance function of velocity fluctuation with respect to time, and is
494 defined as follow:

$$P(f) = \int_{-\infty}^{\infty} r_f(t) e^{-j2\pi ft} dt \quad (22)$$

$$r_f(t) = \langle f'(t)f'(t + \tau) \rangle \quad (23)$$

495 where $P(f)$ represents the PSD as a function of frequency f , r_f the non-normalized
496 autocovariance function of velocity fluctuations and j the imaginary unit. The PSDs achieved
497 by the 2D planar grids under influence of $Re_{Dh}=22 \times 10^3$ are illustrated in Fig. 9. It is worthwhile
498 to mention that the profile was subjected with 10-lapse period of moving average to minimize
499 random noises.

500 Clearly, the energy level demonstrated by the partially-covered grids are much higher
501 compared to the fully-covered counterparts, i.e. an impressive increase of approximately $\times 10^2$,
502 with NG recorded at the lowest energy state. It is noticed that the $P(f)$ of all grid configurations
503 decreases with increasing f , but proceed to surge at higher frequency domains, thereupon a
504 second stage decay. Interestingly, the initial $P(f)$ decay regions exhibit a reduction profile
505 similar to that of Kolmogorov-law, i.e. with exponent approaching $-5/3$. Most grids are
506 observed to follow the decay exponent over a wide range of frequencies except for PCSFG,
507 where the $f^{-5/3}$ is only documented at a narrow band, i.e. approximately between $4\text{Hz} < f < 7\text{Hz}$.
508 Such dissimilarity recorded for PCSFG might indicate the formation of a distinct and unique
509 flow structure that could potentially maintain an intense energy level over wider range of
510 frequencies, which could be beneficial for superior thermal transfer.

511 As previously mentioned, the energy level surges at higher frequency ranges, and is
512 exceptionally pronounced for the partially-covered planar grids. The vertically aligned mid-

513 plane separation gives rise to the formation of dynamic coherent flow structures, thus inducing
514 a distinct velocity fluctuation. Such wake-flow interactions result in a powerful vortex shedding
515 effect, which justifies the excitation at $P(f)$ peak. Moreover, the raised energy levels are
516 observed to span over a wide range of frequencies, with range of PCSFG>PCRG. The
517 phenomenon may imply that partially-covered grids are capable of generating broad array of
518 high energy multilength scale eddies through (i) first stage grid-separation induced turbulence
519 and (ii) second stage plate-fin eddies filtration for an intense vortex shedding process. As
520 PCSFG comprised of different fractal bar thicknesses, there would be greater variations in
521 eddies length scale, hence ampler variety of frequencies. Contrariwise, utilization of fully-
522 covered grids masked the powerful vortex shedding effect, and is further subdued under NG
523 configuration. Surprisingly, the energy profile demonstrated by NG and RG are very much
524 identical, revealing the impact of 2D planar grids in raising the preferable flow energy levels
525 for forced convective heat transfer.

526 Upon closer inspections, it is noticed that the $P(f)$ peaks are recorded at different
527 frequencies, with the lowest realization of $f=18.45\text{Hz}$ by PCSFG, thereupon PCRG, SFG, NG,
528 and RG ranked in ascending order. The differences in frequencies might suggest the presence
529 of an optimum fluctuation frequency f_λ that maximizes heat transfer through forced convection
530 in plate-fin heat sink. As suggested in¹⁷, that velocity fluctuation frequencies at the two
531 extremes of f_λ are ineffective in thermal transfer, as high frequencies ($ff_\lambda \gg 1$) contributed to
532 diffusive effects, whereas low frequencies ($ff_\lambda \ll 1$) appeared as quasi-steady. Moreover, flow
533 fluctuations at high frequency sub-range may be too rapid for any reshuffling of boundary
534 layers to take effect. The particle's trajectory projection illustrated in Fig. 6(a, b) supports the
535 preceding statements, as high frequency fluctuations by PCRG and SFG appear to develop
536 diffusive characteristics in the time-lapsed particle trajectory, causing the extensive
537 contribution of turbulent kinetic energy confined around the shedding frequency to be
538 ineffective in enhancing plate-fin heat transfer. As for PCSFG, the f is presumed to be
539 approaching f_λ , thus resulting in the formation of dense and intense annulus trajectory that
540 directs the turbulent kinetic energy along the boundary layer for maximum agitation. In short,
541 $f_\lambda \approx 18.45\text{Hz}$ provides adequate velocity fluctuations for direct boundary layer restructuring,
542 whilst containing sufficient flow momentum to effectively enhance thermal dissipation.

543 **Conclusion**

544 An in-house developed SPTV system was utilized to investigate the underlining grid-
545 induced flow structures that reinforce positive thermal dissipation of plate-fin array, which was

546 numerically optimized at $\delta=5\text{mm}$ and $l=10\text{mm}$ under $\text{Re}_{Dh}=22.0\times 10^3$. The 2D Nu contour plots
547 were able to reveal augmentations to heat transfer using partially-covered grids, where high Nu
548 was seen at wider coverage range of (δ, l) . Furthermore, the increases of 42.9% and 29.2% in
549 Nu were observed by PCSFG and PCRG, respectively, as compared to control NG. Such
550 enhancements were believed to be stimulated from preferable flow of (i) high U/U_0 , (ii) intense
551 I , (iii) strong (v', w') , (iv) small L/δ , and (v) negative $S(a_x, a_y)$ with (vi) low K for maximum
552 thermal dissipation. These coupling flow dynamics also developed a unique formation of
553 'Turbulent Annulus' which offers a small degree of predictability on turbulence in the periodic
554 annulus oscillation that effectively reshuffle flow boundary layers. Lastly, the PSDs induced
555 by partially-covered grids were of higher orders, with a prominent peak at high frequency sub-
556 range that indicates strong vortex shedding effect. An optimal frequency of $f_{\lambda}\approx 18.45\text{Hz}$ was
557 determined by PCSFG, which was believed to provide adequate turbulent kinetic energy for
558 direct boundary layer restructuring, while maintaining the necessary flow momentum to ensure
559 superior force convective heat transfer of plate-fin heat sink.

560 **Reference**

- 561 1. Bailly, C. & Comte-Bellot, G. *Turbulence* 1-5 (Cham: Springer International Publishing,
562 2015).
- 563 2. Hurst, D. & Vassilicos, J.C. Scalings and decay of fractal-generated turbulence. *Phys.*
564 *Fluids* **19**, 035103 (2007).
- 565 3. Cafiero, G. Greco, C.S. Astarita, T. & Discetti, S. Flow field features of fractal impinging
566 jets at short nozzle to plate distances. *Exp. Therm. Fluid Sci.* **78**, 334-344 (2016).
- 567 4. Cafiero, G. Castrillo, G. Greco, C. S. & Astarita, T. Effect of the grid geometry on the
568 convective heat transfer of impinging jets. *Int. J. Heat Mass Transf.* **104**, 39–50 (2017).
- 569 5. Cafiero, G. Castrillo, G. & Astarita, T. Turbulence properties in jets with fractal grid
570 turbulence. *J. Fluid Mech.* **915**, A12 (2021).
- 571 6. Verbeek, A.A. Willems, P.A. Stoffels, G.G.M. Geurts, B.J. & van der Meer, T.H.
572 Enhancement of turbulent flame speed of V-shaped flames in fractal-grid-generated
573 turbulence. *Combust. Flame* **167**, 97-112 (2016).
- 574 7. Ferko, K. Chiappazzi, N. Gong, J. & Danesh-Yazdi, A.H. Power output comparison of
575 side-by-side fluidic harvesters in different types of fractal grid-generated turbulence. In:
576 *Active and Passive Smart Structures and Integrated Systems XIII* (ed Erturk A). Spie-Int
577 Soc Optical Engineering (2019).
- 578 8. Ferko, K. Chiappazzi, N. Gong, J. & Danesh-Yazdi, A.H. Average power output and the
579 power law: identifying trends in the behavior of fluidic harvesters in grid turbulence. In:
580 *Active and Passive Smart Structures and Integrated Systems XIII* (ed Erturk A). Spie-Int
581 Soc Optical Engineering (2019).
- 582 9. Melina, G. Bruce, P.J.K. Hewitt, G.F. & Vassilicos, J.C. Heat transfer in production and
583 decay regions of grid-generated turbulence. *Int. J. Heat Mass Transf.* **109**, 537–554
584 (2017).
- 585 10. Mazellier, N. & Vassilicos, J.C. Turbulence without Richardson-Kolmogorov cascade.
586 *Phys. Fluids.* **22**, 1-25 (2010).
- 587 11. Seoud, E.R. & Vassilicos C.J. Dissipation and decay of fractal-generated turbulence.
588 *Phys. Fluids* **19**, 105108 (2007).
- 589 12. Teh, A.L. Phoo, Y.W. Chin, W.M. Ooi, E.H. & Foo J.J., Forced convective heat transfer
590 enhancement of 90° bend plate-fin heat sink with grid generated turbulence. *Chem. Eng.*
591 *Res. Des.* **156**, 226–239 (2020).

- 592 13. Hoi, S.M. Chew, I.M.L. Ooi, E.H. & Foo, J.J. SPTV sheds light on fluid dynamics of
593 fractal-induced turbulence over a plate-fin array forced convection. *Exp. Therm. Fluid*
594 *Sci.* under Rev. (2020).
- 595 14. Hoi, S.M. Teh, A.L. Ooi, E.H. Chew, I.M.L. & Foo, J.J. Plate-fin heat sink forced
596 convective heat transfer augmentation with a fractal insert. *Int. J. Therm. Sci.* **142**, 392-
597 406 (2019).
- 598 15. Hoi, S.M. Teh, A.L. Ooi, E.H. Chew, I.M.L. & Foo, J.J. Forced convective heat transfer
599 optimization of plate-fin heat sink with insert-induced turbulence. *Appl. Therm. Eng.* **160**,
600 114066 (2019).
- 601 16. Omilion, A. Turk, J. & Zhang, W. Turbulence enhancement by fractal square grids:
602 effects of multiple fractal scales. *Fluids* **3**, 37 (2018).
- 603 17. Dullenkopf, K. & Mayle, R.E. An account of free-stream-turbulence length scale on
604 laminar heat transfer. *J. Turbomach.* **117**, 401-406 (1995).
- 605 18. Torii, S. & Fuse, H. Effects of the length scale of free-stream turbulence and cylinder
606 size on heat transfer in laminar separated flows. *Exp. Therm. Fluid Sci.* 619-624 (1993).
- 607 19. Sak, C. Liu, R. Ting, D.S.K. & Rankin, G.W. The role of turbulence length scale and
608 turbulence intensity on forced convection from a heated horizontal circular cylinder, *Exp.*
609 *Therm. Fluid Sci.* **31**, 279-289 (2007).
- 610 20. ANSYS® Academic Research, *ANSYS fluent theory guide*. Release 15.0 (2014).

611 **Acknowledgement**

612 The authors would like to express their gratitude to the Malaysian Ministry of Higher Education
613 (MOHE) for the financial support of the present research investigation
614 (Project Code: FRGS/1/2018/TK07/MUSM/02/1). The author would also like to gratefully
615 acknowledge Monash University Malaysia (MUM) for the financial support of the current
616 research project (MUM25929267).

617 **Author Contributions**

618 S.H.C. prepared the initial draft, S.M.H., M.V.T. and J.J.F. revised, refined and edited the
619 manuscript. All authors reviewed the manuscript.

620 **Competing Interest**

621 The authors declare no competing interests.

622 **Additional Information**

623 Correspondence and requests for materials should be addressed to S.H.C. or J.J.F.

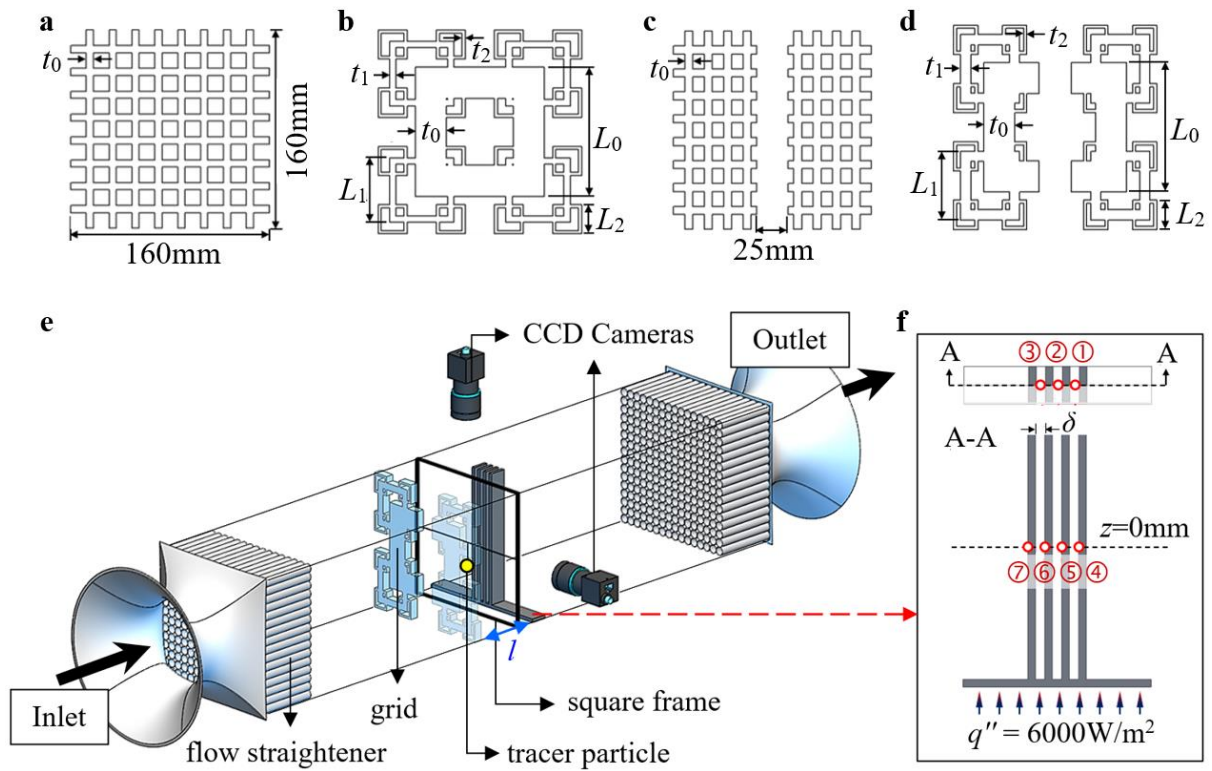


Fig. 1: Schematic diagram of 2D planar space-filling gird of (a) RG, (b) SFG, (c) PCRG, (d) PCSFG, (e) geometrical representation of wind tunnel test section with tracer particle attached on square frame and (f) seven *T*-type thermocouple locations on the plate-fin heat sink.

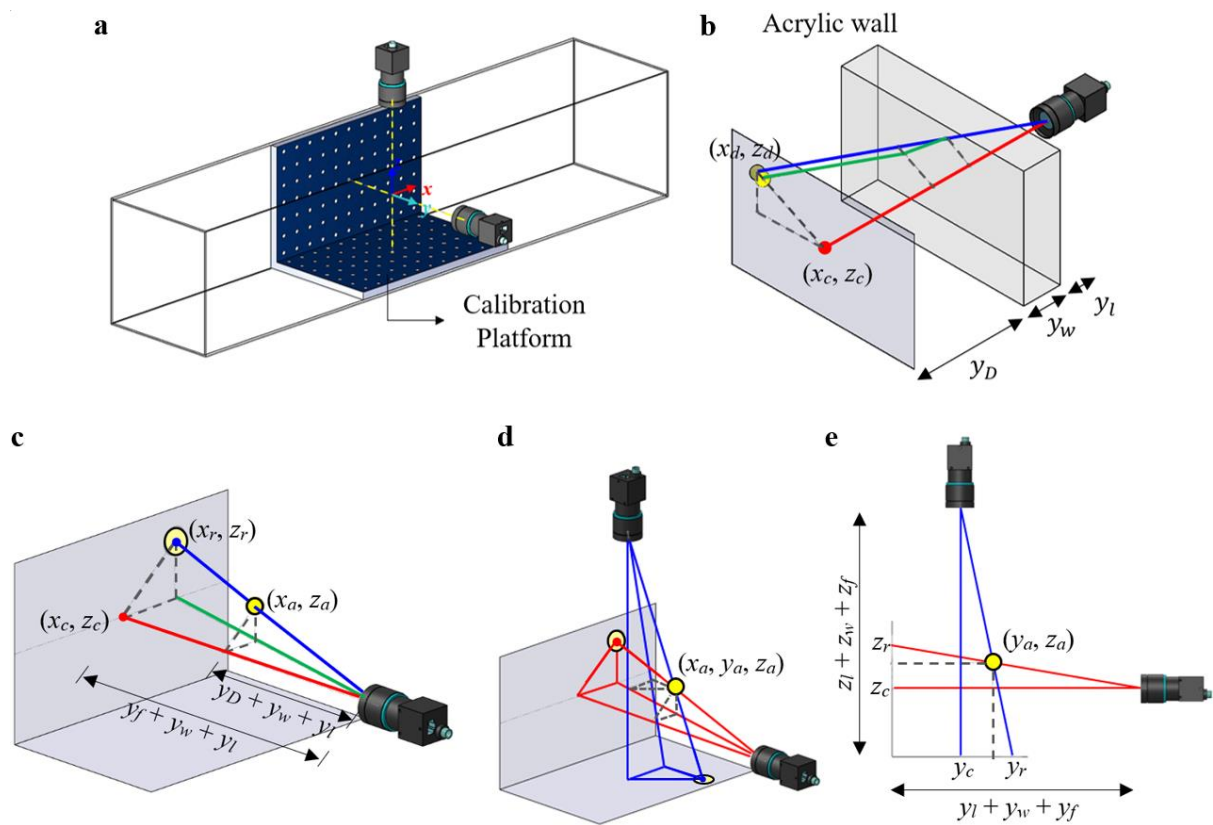


Fig. 2: (a) Alignment of cameras using 7×11 circle array calibration platform, with the Cartesian coordinate set at intersection of cameras' optical axis. (b, c) demonstrate the notation used for refractive and perspective error correction processes. Note that the perspective error influences the (d) projected coordinates of the two cameras, and (e) is the corresponding Y-Z view of the projection.

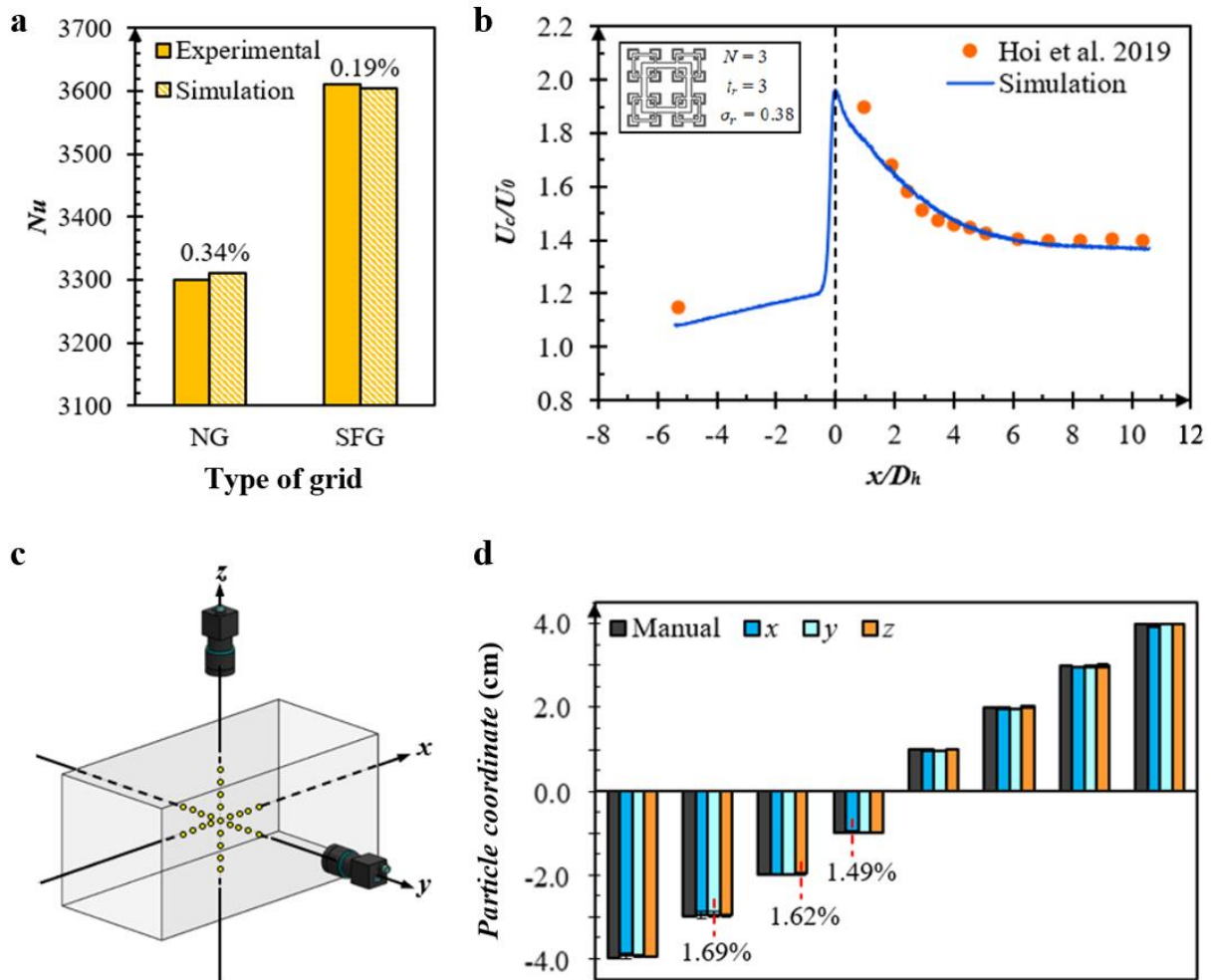


Fig. 3: Top, numerical validation of (a) Nu for NG and SFG, as well as (b) the normalized centreline velocity of fractal grid generated turbulence against Hoi et al. experimental data, viz. [13] and [14], respectively. Bottom, (c) geometrical representation of particle placements in the wind tunnel test section along with (d) the SPTV recorded error margins.

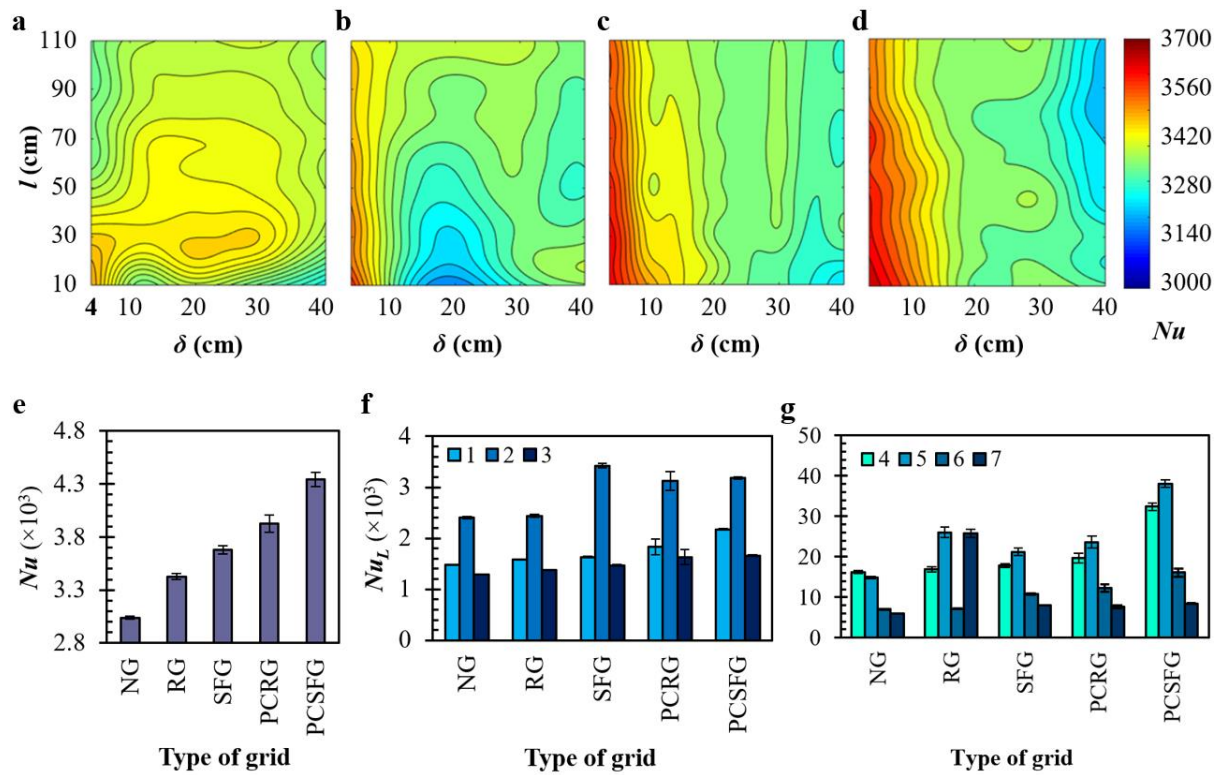


Fig. 4: Top, the numerical 2D Nu contour plot induced by (a) RG, (b) PCRG, (c) SFG and (d) PCSFG as a function of l against δ . Bottom, various grid empirically induced (e) Nu , along with the Nu_L of (f) base section and (g) mid-fin section of plate-fin heat sink.

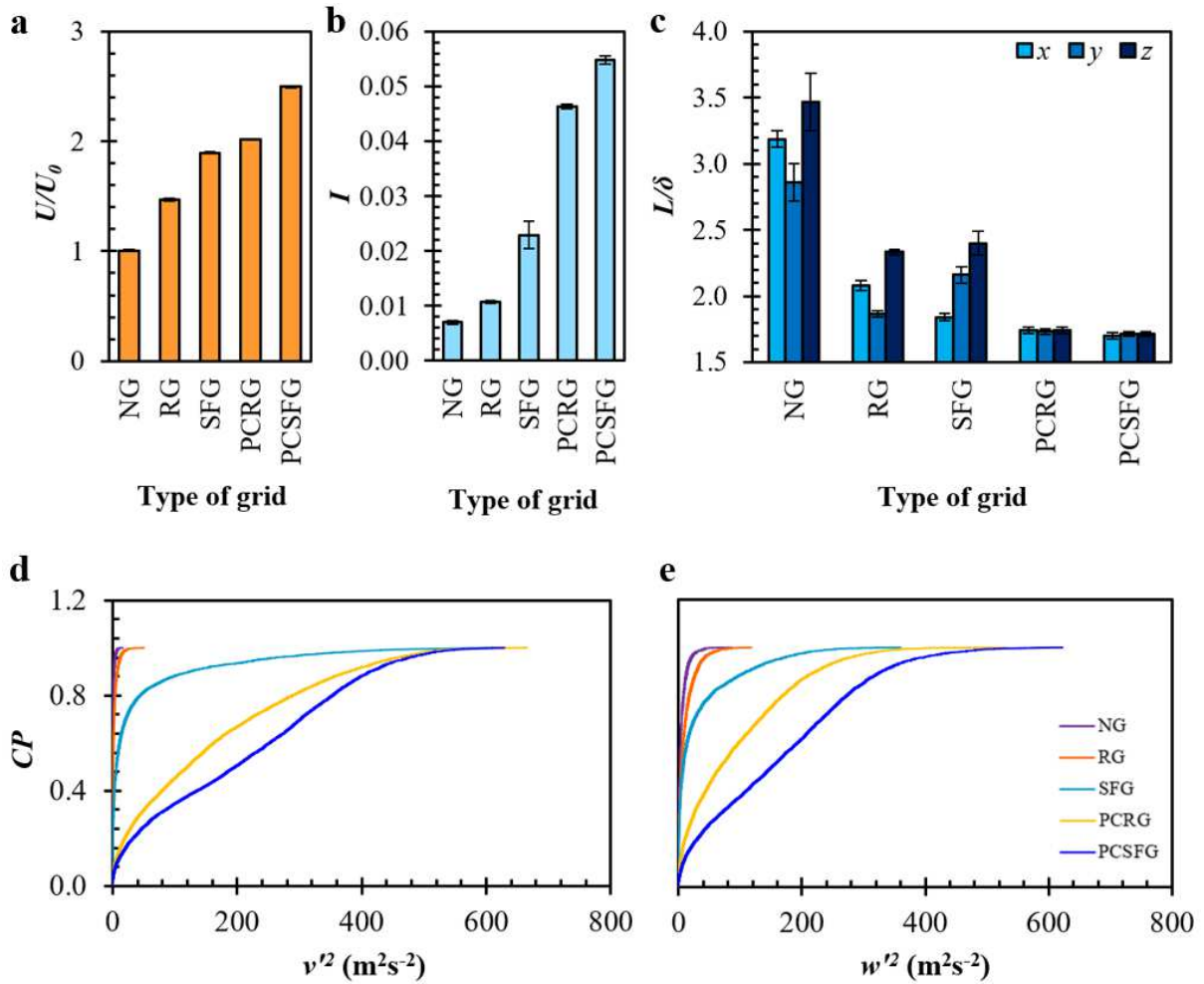


Fig. 5: Various grid induced (a) U/U_0 , (b) I , (c) normalized L/δ in (x, y, z) directional components at centreline $x/D_h=0.125$ and cumulative probability distributions of (d) v'^2 and (e) w'^2 .

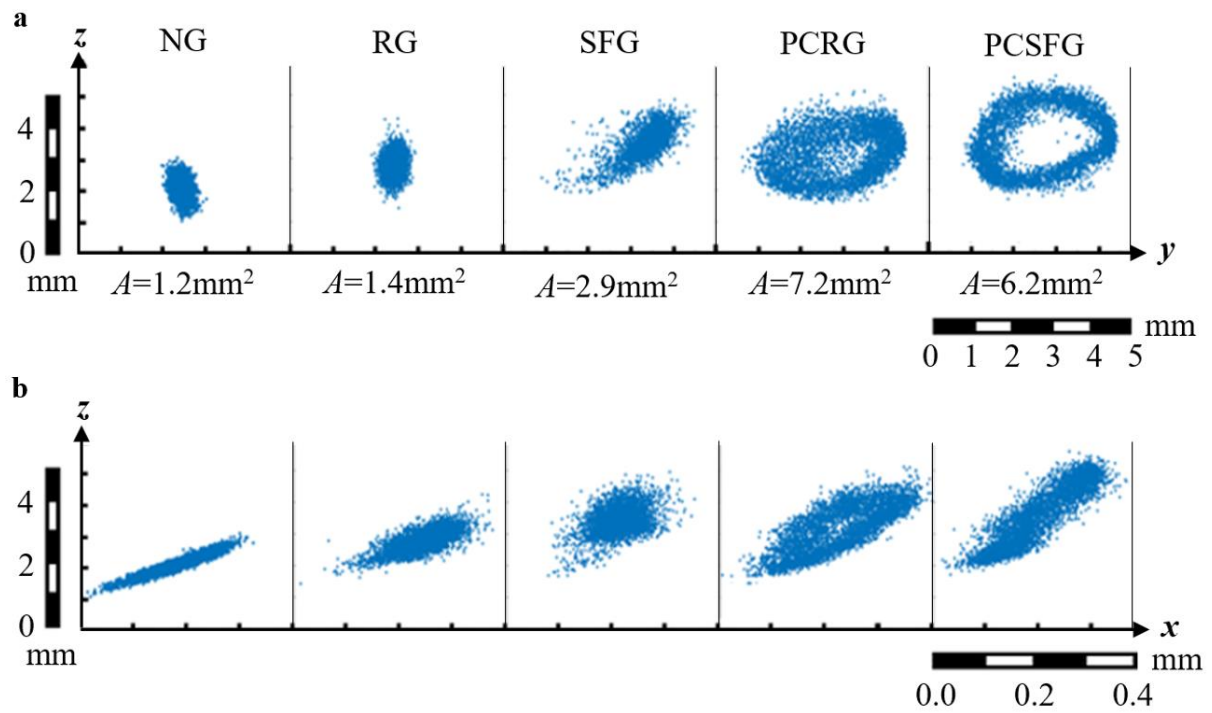


Fig. 6: Trajectory of SPTV tracer particle in the (a) cross-sectional and (b) side view induced from various grid turbulence.

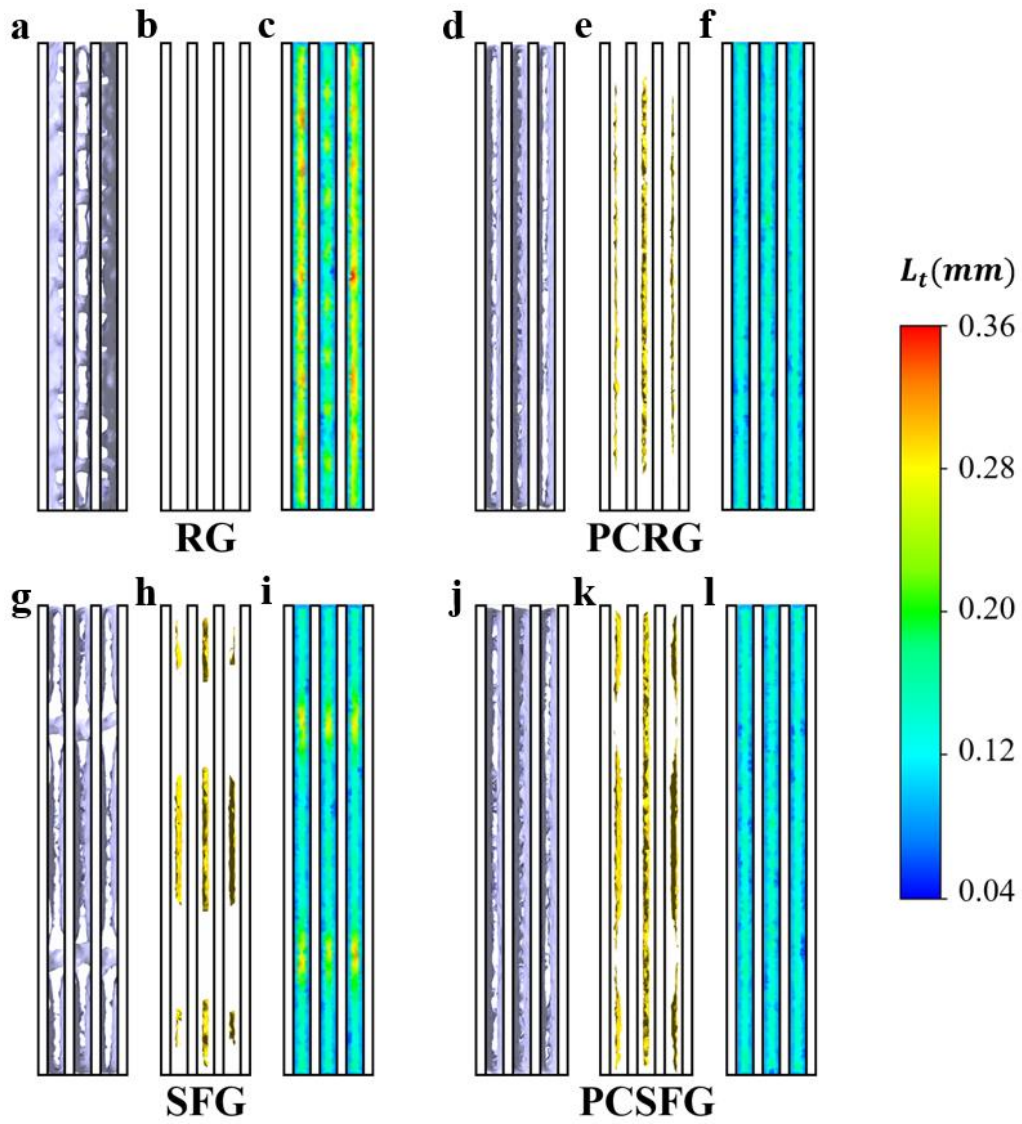


Fig. 7: The cross-sectional isosurface representation of (a, d, g, j) $U/U_0=2.38$, (b, e, h, k) $I=0.33$; and (c, f, i, l) the 2D contour plot of L induced from various grid at $x/D_h=0.125$. Note that $\delta=5\text{mm}$ and $l/D_h=0.0625$.

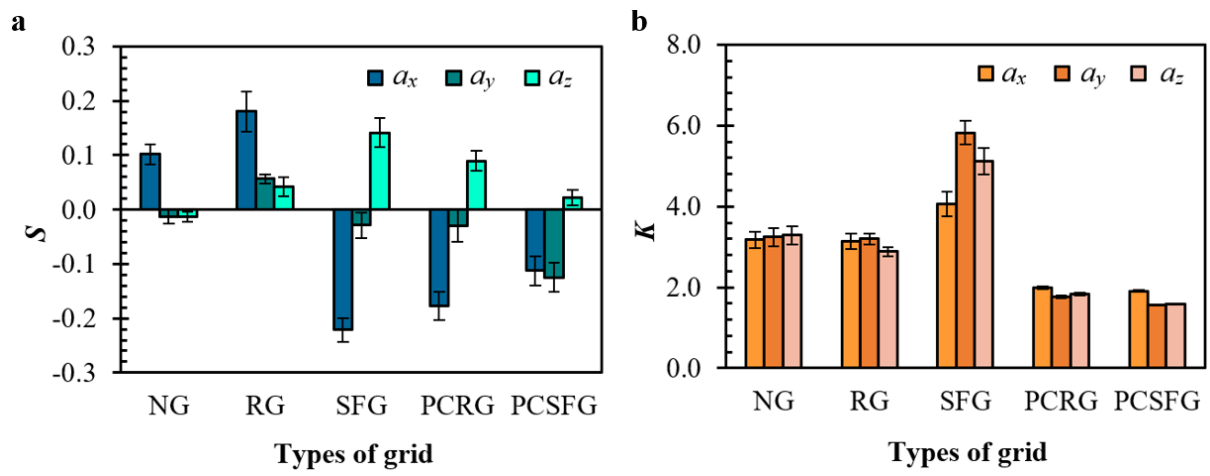


Fig. 8: Various grid induced turbulence on (a) S and (b) K of SPTV particle acceleration in the (x, y, z) directional components.

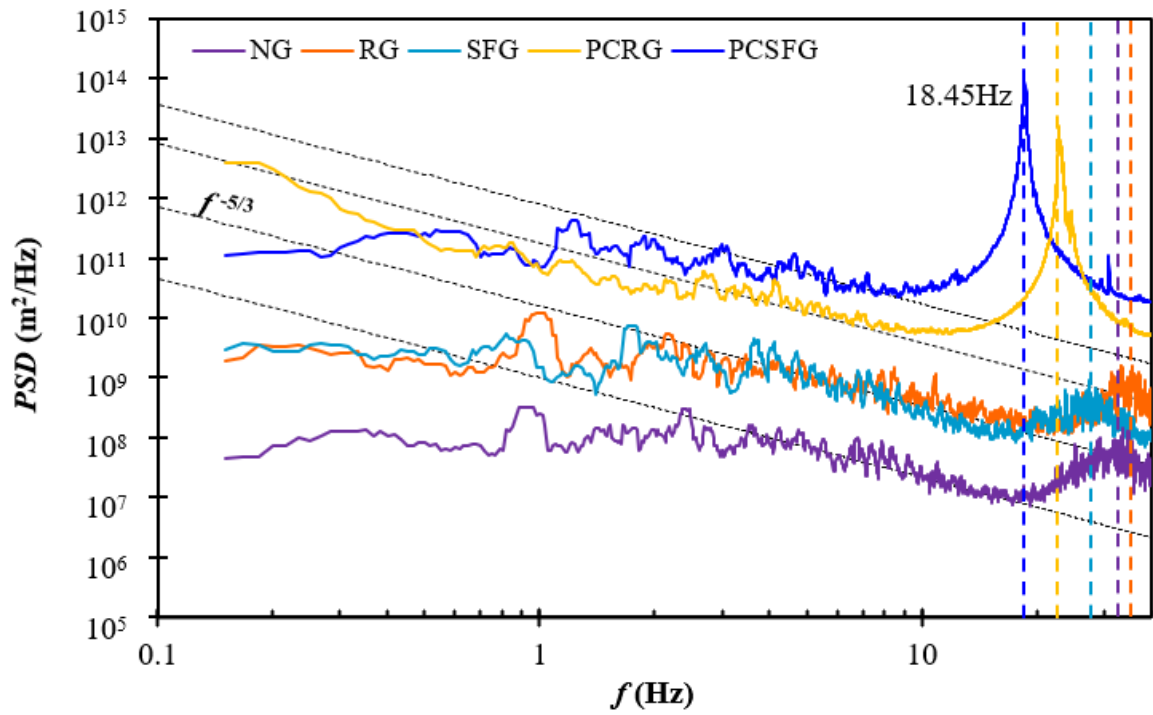


Fig. 9: The 10-lapse period moving averaged PSD of velocity fluctuation induced with various grids at $Re_{D_h}=22.0 \times 10^3$.